Matched Field Processing accounting for complex Earth structure: method and review

Sven Schippkus and Céline Hadziioannou

Institute for Geophysics, University of Hamburg, Germany, Email: sven.schippkus@uni-hamburg.de

This manuscript is a pre-print and has undergone peer-review.

This version has been accepted for publication in Geophysical Journal International.

Matched Field Processing accounting for complex Earth structure: method and review

Sven Schippkus[1] and Céline Hadziioannou[1]

[1] *Institute for Geophysics, University of Hamburg, Germany, Email: sven.schippkus@uni-hamburg.de*

Abstract

Matched Field Processing (MFP) is a technique to locate the source of a recorded wavefield. It is the generalization of plane-wave beamforming, allowing for curved wavefronts. In the standard approach to MFP, simple analytical Green's functions are used as synthetic wavefields that the recorded wavefields are matched against. We introduce an advancement of MFP by utilizing Green's functions computed numerically for Earth structure as synthetic wavefields. This allows in principle to incorporate the full complexity of elastic wave propagation without further manual considerations, and through that provide more precise estimates of the recorded wavefield's origin. We call this approach *numerical MFP* (nMFP). To demonstrate the applicability and potential of nMFP, we present two real data examples, one for an earthquake in Southern California, and one for secondary microseism activity in the Northeastern Atlantic and Mediterranean Sea. In addition, we explore and clarify connections between localisation approaches for the ambient seismic field, real world limitations, and identify key areas for future developments. To increase the adoption of MFP in the seismological community, tutorial code is provided.

Keywords

Seismic noise, Seismic Interferometry, Interferometry, Wave propagation

1 Introduction

The ambient seismic field has become an attractive target of seismological studies over the last two decades (Nakata et al., 2019). Interferometry of this complex wavefield, combined with increased

station density, has enabled detailed studies of Earth's structure (e.g., Shapiro et al., 2005; Lu et al., 2018; Schippkus et al., 2018) and its temporal changes (e.g., Brenguier et al., 2008; Hadziioannou et al., 2011). Such studies rely most commonly on seismic wavefields generated by the interaction between the oceans and the solid Earth, so-called microseisms. Understanding the exact mechanism for this interaction has been a challenge for more than half a century (Longuet-Higgings, 1950; Hasselmann, 1963; Ardhuin et al., 2015) and some open questions remain, e.g., about the emergence of Love waves in the secondary microseism (Ziane & Hadziioannou, 2019; Gualtieri et al., 2020). More recently, other sources such as trains (Fuchs et al., 2017; Brenguier et al., 2019; Liu et al., 2021), wind turbines (Stammler & Ceranna, 2016; Hu et al., 2019), direct wind-land interaction (Johnson et al., 2019), rain (Dean, 2019), and rivers (Burtin et al., 2008; Smith & Tape, 2019) have become the focus of several studies investigating high-frequency seismic noise.

To study all of these sources in detail and understand their mechanisms, precise knowledge of their locations is necessary. Dense installations of seismic stations near known sources can provide intriguing insight into the sources' interactions with the solid Earth (Riahi & Gerstoft, 2015), and can give evidence for previously unrecorded interactions (Schippkus et al., 2020). Installations like these are not widely available, though. For other sources, it may not be technically feasible to install stations close to all expected source locations, e.g., in the deep oceans to study ocean microseisms or in the Earth's subsurface. Beyond the interest in the fundamental principles of seismic wave generation by different sources, studies that rely on interferometry of the ambient seismic field to gain knowledge about Earth's structure ideally incorporate a priori knowledge of source locations to account for the potential bias introduced by their spatial distribution (Fichtner et al., 2017; Sergeant et al., 2020).

Strategies of earthquake seismology to locate seismic sources, such as travel-time inversion, are not applicable to ambient seismic noise due to the complexity of the analysed wavefield. There is not one single dominant source (e.g., an earthquake or explosion) that results in clearly identifiable and thus exploitable phase arrivals in seismograms across several stations. In other words, methods that rely heavily on data abstraction may not be useful (Li et al., 2020). Instead, strategies have emerged that aim to quantify the angle of arrival of seismic energy in recorded seismograms emitted by sources of unknown type. In the following, we give a brief overview of the current methods for locating sources of the ambient seismic field.

Polarization analysis exploits the particle motion of the seismic wavefield at one location $\vec{x}_j$, resolved by three-component seismometers (Fig. 1a, e.g., Schimmel & Gallart, 2003). Depending

on the analysed wave type, the particle motion gives an indication of the angle of arrival. When combining results from multiple stations, this analysis can be used to triangulate the source location $\vec{x}_s$ (e.g., Schimmel et al., 2011). However, a number of assumption have to be made, e.g., great-circle propagation, as well as proper identification and clear separation of wave types. This approach can be a first step in understanding the recorded wavefield, but is often quite tricky in practice, especially on recordings of ambient seismic noise (Gal & Reading, 2019).

Beamforming is a source localisation approach based on the assumption that seismic waves propagating across seismic arrays can be treated as plane waves, which is valid if wavelengths are much larger than the aperture of the array (Fig. 1b). To test whether a candidate plane wave - characterised by its horizontal slowness or equivalently arrival angle and apparent velocity - was recorded on the array, expected relative time delays $\Delta t(\vec{x}_j, \vec{x}_k)$ between the stations are computed and corrected for. This is called delay-and-sum beamforming, where each seismogram is shifted in time and summed together, forming the beam (Rost & Thomas, 2002). The quality of the beam is evaluated, giving the so-called beampower. Other formulations of this method exist, e.g., an equivalent cross-correlation approach (Ruigrok et al., 2017). Beamforming has been widely adopted by the seismological community and is currently the standard tool for identifying sources of the ambient seismic field (Gal & Reading, 2019, and references therein). Recent advances focus on incorporating three-component seismograms (Riahi et al., 2013; Juretzek & Hadziioannou, 2016, 2017), avoiding bias introduced by averaging across broad frequency bands (Gal et al., 2014), or estimating surface wave anisotropy directly from beamforming (Löer et al., 2018). Beamforming has its main advantages in computational speed, little if any data processing, and high resolution in time. Its main drawbacks all result from the plane-wave assumption: sources have to be far from the array, the wavefield has to be strictly coherent across stations, and the array geometry limits the resolution capabilities (Rost & Thomas, 2002). For a recent review of beamforming and polarization analysis see Gal & Reading (2019).

A new source localisation strategy based on seismic interferometry has been introduced in recent years as an attractive alternative, sometimes referred to as kernel-based source inversion (Ermert et al., 2016). The goal of this approach is not to determine the angle of arrival, but to directly quantify the distribution of seismic sources in space. Interferometry of the ambient seismic field recorded on multiple stations gives new wavefields, propagating to and from the respective reference stations (Fig. 1c, Aki, 1957; Wapenaar et al., 2010; Campillo & Roux, 2015; Fichtner et al., 2017). An inhomogeneous distribution of sources results in asymmetric cross-correlation functions, indicated

by the thickness of the wave fronts in Fig. 1c (Paul et al., 2005). In practice, this asymmetry is usually quantified by comparing the causal and acausal part of each correlation function. In the interferometry-based approach, synthetic cross-correlation functions are computed for a given source distribution and compared against cross-correlation functions from real data. The mismatch between the two is evaluated (e.g., by quantifying amplitude asymmetry), the source model perturbed, and a best-fit source distribution is found via gradient descent in an iterative manner (Ermert et al., 2016). Recent work has focused on improving efficiency (Igel et al., 2021b), the mismatch measure (Sager et al., 2018), or expanding the method to multiple frequencies (Ermert et al., 2021). The advantages of this approach are the stability of results, not as strict requirements on station geometry, and a comprehensive theoretical foundation. Its disadvantages lie in computational cost, treatment of recorded data and related introduction of assumptions, and loss of temporal resolution.

Another approach that has gained some popularity in seismology in recent years is Matched Field Processing (MFP). MFP is the generalisation of beamforming to allow arbitrary wavefronts (Baggeroer et al., 1993). This approach has been developed in ocean acoustics, where coherency of the wavefield emitted by transient sources is high even for stations far away. Candidate sources are defined in space and absolute travel times $t(\vec{x}_j, \vec{x}_s)$ are computed based on true distance to the source (Fig. 1d). Synthetic wavefields are computed for these travel times and matched against the recorded wavefield. In the seismological context, MFP has been applied succesfully on local (Corciulo et al., 2012; Umlauft & Korn, 2019; Umlauft et al., 2021) and regional scale (Gal et al., 2018). Recent developments in MFP include the development of different beamformers (e.g., Zhu et al., 2020), improved estimation of travel times (Gal et al., 2018), or estimating synthetic wavefields empirically (Gibbons et al., 2017). MFP is an attractive strategy for source localisation of the ambient seismic field. It allows for curved wavefronts, is based on only few assumptions, requires no intermediate step such as pre-processing of recordings, and retains computational efficiency. While the plane-wave assumption is not required in MFP, coherency of the wavefield across stations is still necessary for good results. This poses challenges when analysing recordings for stations that are not close together, and especially so for ambient seismic noise.

In this paper, we introduce an advancement of MFP to incorporate Earth structure and account for the complexity of seismic wave propagation. In the following, we introduce the standard MFP approach, demonstrate its shortcomings, and present our solution by incorporating more realistic Green's functions. We discuss implications of our approach, strategies to cope with them, how different disciplines and localisation approaches intersect, and finally demonstrate the applicability

of our approach on two real data examples. In line with the informative nature of this paper, we provide broader context and discuss ideas as they become relevant instead of deferring such considerations to a separate discussion section.

2 Matched Field Processing

The MFP algorithm is straight-forward: For a given potential source location, a synthetic wavefield is computed and matched against the recorded wavefield, i.e., the seismograms, taking coherency of the wavefields across stations into account. This match is evaluated and compared against other potential source locations. The potential source location with the highest score or beampower (representing the best-matching synthetic wavefield) is the resolved source location.

More precisely, spectra $d(\omega, \vec{x}_j)$ are computed from the recorded seismograms at each receiver position $\vec{x}_j$. The cross-spectral density matrix is computed as

$$K_{jk}(\omega) = d^*(\omega, \vec{x}_j) d(\omega, \vec{x}_k), \tag{1}$$

with $*$ denoting the complex conjugate. $K_{jk}(\omega)$ holds all information about the recorded wavefield and encodes its coherency across stations; it contains the cross-correlations of the seismograms from all station pairs.

The synthetic wavefield, i.e., the seismograms expected at each station from the candidate source, is represented through synthetic spectra $s(\omega, \vec{x}_j, \vec{x}_s)$, with $\vec{x}_s$ the source position and $\vec{x}_j$ the receiver position. In principle, these could be estimated in the time domain, but MFP computations are done in frequency domain for simplicity and computational speed. More on how these are computed in practice in section 2.1 and onwards.

The match of the two wavefields represented through $K_{jk}(\omega)$ and $s(\omega, \vec{x}_j, \vec{x}_s)$ is then estimated through a so-called beamformer or processor. The most straight-forward beamformer is the conventional beamformer, which in its most compact form in vector notation is often written as (e.g., equation 25 in Baggeroer et al., 1993)

$$B = \mathbf{s}^* \cdot \mathbf{K} \cdot \mathbf{s}, \tag{2}$$

with B the beampower score for a potential source location. In literature, this beamformer is sometimes called Bartlett processor, although the origin of this name is unclear (e.g., Gal & Reading, 2019), linear beamformer (e.g., Baggeroer et al., 1993), or frequency-domain beamformer (DeMuth,

1977). We express B more explicitly, for clarity as

$$B = \sum_{\omega} \sum_{j} \sum_{k \neq j} s_j^*(\omega, \vec{x}_j, \vec{x}_s) K_{jk}(\omega) s_k(\omega, \vec{x}_k, \vec{x}_s). \tag{3}$$

We exclude auto-correlations ($k = j$), as in Bucker (1976), because they carry "noise", i.e., the incoherent parts of the wavefield (Soares & Jesus, 2003) and provide no useful additional information. Auto-correlations scale the retrieved beampowers by recorded energy, which is not necessarily caused by a higher signal-to-noise ratio (SNR). Here, signal refers to those parts of the ambient seismic field that are (often weakly) coherent across stations.

Other estimators of beampower exist, and their development is an active field of research (e.g., Capon, 1969; Schmidt, 1986; Cox et al., 1987; Cox, 2000; Gal et al., 2014; Zhu et al., 2020). Beamformers are often classified into conventional (eq. 3), adaptive (e.g., Capon, 1969; Cox et al., 1987; Cox, 2000) and sub-space beamformers (e.g., Schmidt, 1986). Adaptive beamformers aim to increase resolution of the beampower distribution by increasing sensitivity to signal, but inherently rely on high SNR. The increased resolution is also accompanied by increased computational cost, e.g., the Capon beamformer involves computing the inverse of $K_{jk}(\omega)$(Capon, 1969). Sub-space detectors such as MUSIC (Schmidt, 1986) involve computation of the eigenvectors of $K_{jk}(\omega)$, and making a selection of those for further computations based on which eigenvectors contribute to the signal and which are "noise". Corciulo et al. (2012) used a similar approach and were able to resolve multiple sources this way. One of the expressed goals of the approach we introduce in this paper is to be able to locate sources of ambient seismic noise, and as such SNR is by definition low. Beamformers beyond the conventional beamformer may not be appropriate for this, because they either require high SNR or a choice of what part of the cross-spectral density matrix is signal and what is "noise". Krim & Viberg (1996) have addressed the question of which beamformer performs best under what circumstances for standard MFP. A detailed analysis of beamformer performance in the context of our approach we introduce here is beyond the scope of this paper.

2.1 Synthetic wavefield in the standard approach

In practice, assumptions and simplifications about structure and wave propagation have to be made in order to compute the synthetic wavefields $s(\omega, \vec{x}_j, \vec{x}_s)$ that the recorded data are matched against. In most seismological and almost all ocean acoustics applications so far, simple analytical Green's functions of the form

$$s(\omega, \vec{x}_j, \vec{x}_s) = e^{-i\omega t(\vec{x}_j, \vec{x}_s)}, \tag{4}$$

are used, with $t(\vec{x}_j, \vec{x}_s)$ the travel time of the investigated wave between source and receiver (Fig. 1d). In some seismological studies, the addition of an amplitude term $A(\vec{x}_j, \vec{x}_s)$ that accounts for geometrical spreading and/or inelastic attenuation has been discussed (Corciulo et al., 2012; Bowden et al., 2021). The goal of such a term would be to increase the accuracy of the synthetic wavefield by incorporating some of the seismic waves' propagation behaviour. Neglecting the amplitude term entirely, as is usually done, makes standard MFP equivalent to delay-and-sum beamforming without the plane-wave assumption (Bucker, 1976). More on this in section 2.4.

For a single stationary source in an acoustic, isotropic, homogeneous medium, i.e., with constant velocity $v = const$ and only straight-ray propagation of a single phase (the simplest possible study target), the travel time is simply $t(\vec{x}_j, \vec{x}_s) = \Delta x / v$. Estimating travel times requires prior knowledge of v and the assumption that $v = const$ is a good approximation of the medium. In seismology, this approach has been successfully demonstrated on local scale (e.g., Corciulo et al., 2012; Umlauft & Korn, 2019; Umlauft et al., 2021), where propagation effects due to heterogeneous Earth structure can be neglected. Without any prior knowledge of the velocity structure, another approach is to treat v as an additional dimension in the parameter space that needs to be explored, though this can become computationally quite expensive and may require sampling strategies other than a standard grid search (Gradon et al., 2019).

On regional scale, Gal et al. (2018) estimated $t(\vec{x}_r, \vec{x}_s)$ from already available phase velocity maps using Fast Marching Method (Sethian, 1999), which accounts for off-straight-ray propagation of surface waves, and by that incorporating some complexity of wave propagation in complex Earth structure. This approach also inherently incorporates frequency-dependent effects, i.e., $t(\vec{x}_r, \vec{x}_s)$ becomes $t(\vec{x}_r, \vec{x}_s, \omega)$. Gal et al. (2018) used this to study the primary (~16 sec. period) and secondary (~8 sec. period) microseism separately by estimating phase travel times from their respective phase velocity maps. They assume that surface waves are dominant in the microseism frequency band and are only recorded on their respective component (Love on transverse, Rayleigh on radial). This assumption is reasonable and commonly made when analysing ocean microseism (Nakata et al., 2019), but may not always be appropriate depending on the study target. Incorporating multiple phases (e.g., a mix of body and surface waves) at the same frequency is not straight-forward with the standard approach and clearly requires further assumptions about the number of phases and their respective travel times, increasing the parameter space considerably. Furthermore, when investigating frequencies at which the identification of wave types may be challenging, this strategy potentially misses or misattributes important information in the recorded wavefield and may bias

results. Approaching the complexity of wave propagation in real Earth structure in this manner requires numerous manual interventions, as outlined above, and could therefore become impractical in wider use.

2.2 Numerical synthetic wavefields for complex Earth structure

We propose to use Green's functions computed numerically for Earth structure directly as the synthetic wavefield $s(\omega, \vec{x}_r, \vec{x}_s)$ ("numerical MFP" or nMFP) instead of the analytical form described above (eq. 4, "standard approach"). Effects such as dispersion and multiple wave types are then inherently accounted for, even for simple 1D media. If the Green's function are computed for a 3D Earth, further effects such as focusing and defocusing, wave-type conversion, and coupling can all be accounted for, increasing the precision of this approach further.

We demonstrate our method with synthetic examples for a broadband and a narrowband explosion source (Fig. 2). The setup consists of two small arrays of three stations each that record the wavefield emitted by a seismic source located at the surface between them. The medium is a 3D axisymmetric Earth (Nissen-Meyer et al., 2014), based on PREM (Dziewonski & Anderson, 1981). The "recorded" seismograms are computed for the same model and incoherent noise is added. With the standard MFP approach (assuming $t(\vec{x}_r, \vec{x}_s) = \Delta x/v$), locating the source precisely is quite challenging for both broad- and narrowband sources (Fig. 2a, c). The resolved location is clearly sensitive to the chosen velocity of the medium v. When the chosen velocity is too low, the resolved source lies further away than the real source. When it is too high, the resolved source lies closer. This applies to both broadband and narrowband sources (Fig. 2a, c). For the broadband source, the highest frequency available in the numerical Green's functions is 0.2 Hz. The error in location introduced for $v = 3.0$ km/s is smaller for the broadband source than for the narrowband source. This occurs, because the broadband wavefield contains phases that are of different type and travel with different velocities, and $v = 3.0$ km/s is a good estimate for at least some of them. For the narrowband wavefield, which contains mainly Rayleigh waves at 0.13-0.15Hz, $v = 3.0$ km/s is already clearly too slow. For surface waves in particular, a different choice of velocity v for each analysed frequency band would seem appropriate due to their dispersive nature (Gal et al., 2018).

With Green's functions computed numerically for the same Earth structure, the location of the source is resolved precisely for both broad- and narrowband sources (Fig. 2b, d). This is unsurprising, given that we are essentially matching the synthetic wavefield against itself with some noise. But this is also exactly the intent behind the approach: matching the recorded wavefield with a more

realistic synthetic wavefield. Our simple synthetic tests show that the standard approach can be imprecise for locating realistic sources in slightly complex media, even under ideal conditions, and is highly dependent on choosing the correct velocity. With nMFP, we do not have to consider frequency-dependent effects explicitly as long as the numerical Green's functions applied are a good representation of elastic wave propagation.

MFP for narrowband sources results in prominent side lobes of beampower, regardless of approach (Fig. 2c,d). These are interference patterns that emerge because of the near-monochromatic nature of the wavefield. The exact shape and position of sidelobes depends on the station distribution and wavelength of the investigated wave, while the correct location does not. Sidelobes will be suppressed, if a wide frequency band is used (Fig. 2a,b) or several runs of MFP for narrow neighbouring frequency bands are stacked (Umlauft et al., 2021). MFP originated as a narrowband localisation technique (Bucker, 1976) and has been adopted for broadband sources thereafter (e.g., Baggeroer et al., 1993; Brienzo & Hodgkiss, 1993; Soares & Jesus, 2003), where the suppression of sidelobes plays a role. This has some implications for the resolution capability of MFP, which depends heavily on whether the analysed source emits a wide frequency band or not. These interference patterns can also be thought of as a trade-off between spatial and frequency resolution of MFP. Using more precise Green's functions has in principle no impact on this.

The basic idea of incorporating more realistic Green's functions in MFP is not new. In ocean acoustics, waveforms are coherent across large distances due wave propagation being focused in the SOFAR channel, but MFP results can be highly sensitive to acoustic wave velocities (Tolstoy, 1989), similar to what we have shown in Figure 2. Bathymetry and multiple reflections may complicate the recorded wavefield even further and impact MFP performance significantly, and thus should ideally be incorporated (e.g., D'Spain et al., 1999). For elastic waves in solid Earth structure, further effects would need to be considered, as described above. One approach to this is empirical Matched Field Processing (Gibbons et al., 2017). Gibbons et al. (2017) estimate empirical Green's functions for each station from recordings of known sources by computing the principal eigenvector of the covariance matrix of the incoming wavefield for two nearly identical sources. They have demonstrated their approach in the context of mining blasts. The obvious limitation is that such template sources are required, which allows its application only for certain scenarios. This approach inspired the name for our approach (numerical MFP, nMFP), as we estimate Green's function numerically instead of empirically.

nMFP is not limited to recorded template sources. Using numerically computed synthetic wave-

fields, we can place candidate sources wherever we want. Our approach is then mainly limited by the accuracy of the numerical model and computation strategy. Improving MFP in this way has only become possible recently thanks to efforts by other authors to improve the computation of databases of Green's functions for modelled Earth structure and provide them to the community (e.g., Nissen-Meyer et al., 2014; van Driel et al., 2015; Krischer et al., 2017; Heimann et al., 2017). Computing Green's functions for complex Earth structure is expensive, which is why we rely in our analysis on pre-computed databases using *instaseis* (van Driel et al., 2015). Green's functions databases for realistic Earth structure up to frequencies of the secondary microseism are available for download at IRIS-DMC (Hutko et al., 2017) or Pyrocko Green's Mill (Heimann et al., 2017).

2.3 On amplitudes in MFP

The standard approach does not include an amplitude term. When it is incorporated, it ideally describes the two dominant contributions to amplitudes for geometrical spreading and inelastic attenuation (e.g., Bowden et al., 2021). Computing both requires assumptions about wave type and the attenuation properties of the Earth, again increasing the parameter space. Bowden et al. (2021) show in a synthetic example that first applying and later correcting for this amplitude term does not improve source locations compared to neglecting it from the beginning. It merely tests whether the assumed wave type and quality factor are correct, which poses the danger that wrong assumptions may bias results in real data studies, but also opens the opportunity to constrain anelastic properties of the Earth, if the source locations are already well-known. More importantly though, Bowden et al. (2021) also showed that computing MFP results including the amplitude term in the synthetic Green's function without correcting for it is equivalent to mapping out the sensitivity kernel for the given station-source distribution. As the authors have pointed out, MFP and interferometry-based localisation are closely connected (more on this in section 2.4). MFP without correcting for amplitudes is not useful for directly locating sources (as the highest score is no longer necessarily at the source location), but can be an appropriate starting model for the interferometry-based strategy (Igel et al., 2021a).

A strategy similar to the interferometry-based scheme, where the source strength at a position is perturbed and the fit between model and data is evaluated, is not viable for MFP itself. The beampower at a potential source location scales linearly with the absolute amplitudes of the recorded seismograms. This is the case, even if the match in amplitude decreases, because MFP is ultimately summing over correlations of waveforms. For this reason, other measures of waveform-similarity

that account for a mismatch in amplitude are commonly applied in other approaches, e.g., in full waveform inversion (Yong et al., 2019, and references therein). Accounting for this behaviour directly in MFP would require significant changes to how beamformers are designed.

Therefore, a strategy is required to correct for amplitude terms. Numerically computed Green's functions for complex Earth structure inevitably contain amplitude terms. Several approaches may appear reasonable to correct for them: correcting for amplitude decay (Fig. 3b), time-domain normalisation (Fig. 3c), and spectral whitening (Fig. 3d). Without any treatment of amplitudes, the beampower distribution is heavily biased by distance to stations (Fig. 3a). This effect is more pronounced compared to Bowden et al. (2021), because our Green's functions also contain body waves. Only a zoomed-in view allows to see the distribution of beampowers with a linear colorscale. The retrieved source location without amplitude treatment is close to one of the stations nearest to the actual source at the center.

Applying a correction factor for geometrical spreading of surface waves as has been demonstrated by Corciulo et al. (2012) corrects for some but not all of the amplitude bias (Fig. 3b). The beampower peak is still found near a station, because body waves are not corrected for. It is not clear how a single correction term could be designed to correct for both body and surface waves simultaneously. When we neglect the near-station beampowers, we find a local maximum (small red circle) near the correct source location. We are not able to resolve the source location correctly. For now, we advise against application of a correction term for amplitude decay, because it requires assumptions about wave type and the medium's inelastic properties, opening up room for error and bias as demonstrated here. When synthetic Green's function contain only a single wave type, applying a correction term is a viable strategy as shown by Bowden et al. (2021). In real applications and without prior knowledge of the source location (which defeats the purpose of MFP), such bias is not trivial to resolve. More drastic approaches to dealing with amplitude-induced bias are necessary.

Time-domain normalisation aims to completely remove the impact of amplitudes by converting the synthetic wavefields to time domain $s(t, \vec{x}_j, \vec{x}_s)$ and dividing those by their maximum amplitude. With this approach, we resolve the beampower peak close to the true source (Fig. 3c), but introduce ripple-shaped artefacts in the entire beampower distribution. Time-domain normalisation is only then equivalent to properly removing the effect of amplitude decay, if waveforms did not change their shape across stations. Elastic wave propagation in realistic Earth structure results in the emergence of different phases depending on source-receiver distance, changes to the waveforms due to dispersion, as well as their amplitudes being affected differently by decay. These effects introduce the observed

pattern, which is undesirable.

Spectral whitening or frequency-domain normalisation is the process of dividing the frequency spectrum by its amplitude spectrum, a technique commonly applied in processing of ambient seismic noise records for interferometry (Bensen et al., 2007; Fichtner et al., 2020). Neglecting amplitudes as done in the standard approach is equivalent to whitening of synthetic Green's functions. In fact, whitening of the synthetic wavefield is applied in early formulations of standard MFP (equation 24 in Baggeroer et al., 1993). In the context of interferometry of the ambient seismic field, whitening is often performed with a water-level or smoothed amplitude spectrum to stabilise the procedure numerically and not over-emphasize frequencies that carry no useful information (Bensen et al., 2007). Because we treat the synthetic spectra only, we are not concerned with smoothing of the amplitude spectrum before division and artefacts that whitening may introduce in real data and directly perform whitening as

$$s_{\text{white}}(\omega, \vec{x}_j, \vec{x}_s) = \frac{s(\omega, \vec{x}_j, \vec{x}_s)}{|s(\omega, \vec{x}_j, \vec{x}_s)|}. \tag{5}$$

This approach successfully retrieves the correct source location and does not appear to introduce any unwanted biases (Fig. 3d).

From our tests, whitening the spectra of the synthetic wavefields (Fig. 3d) appears to be the most advantageous approach, and follows the original formulation of MFP (Baggeroer et al., 1993). It introduces no alteration of the recorded data, eliminates attenuation and spreading effects, removes potential issues caused by source strength, and successfully retrieves the true source location. With this approach, individually acting sources are weighted equally likely, regardless of distance to the receivers, as long as their wavefields are well-recorded on all stations. This may not always be an advantage, e.g., in global-scale studies, where the convergence of the wavefield at the source's antipode can introduce bias. By whitening we also lose the ability to, in principle, constrain anelastic parameters of the Earth, but it is not clear to us how that could be approached for numerically computed Green's functions that contain all wave propagation effects.

2.4 Naming conventions and conceptual approaches to MFP

To illustrate how literature from multiple discplines intersects, we want to take a moment to clarify different naming conventions and how MFP can be understood conceptually in different ways.

In this paper, we use language that describes the results of MFP as the distribution of beam-power retrieved from matching recorded wavefields with synthetic wavefields or Green's functions

$s(\omega, \vec{x}_j, \vec{x}_s)$ for candidate source locations. This language, particularly *Green's functions*, is natural for seismologists (e.g., Gibbons et al., 2017; Umlauft & Korn, 2019), though rarely also used in ocean acoustics studies (e.g., Li et al., 2021). In ocean acoustics, other terminology is more common for some of these concepts. $s(\omega, \vec{x}_j, \vec{x}_s)$ is instead sometimes called *steering vector*, expressing the idea that the array is "steered" towards the source during beamforming or MFP, or *replica vector*, communicating that the vector represents a replica of the expected wavefield (Baggeroer et al., 1993). The distribution of beampowers may be called *ambiguity surface* (Bucker, 1976), intended to express the emergence of sidelobes for narrowband sources (Fig. 2c,d).

Both the seismological and ocean acoustics communities understand MFP as matching of wavefields; this idea is the original concept introduced by Bucker (1976), and gives an intuitive understanding of the physics involved. Above, we mentioned that array beamforming for plane waves is a special case of MFP. For plane-wave beamforming, Green's functions of the form $s(\omega, \vec{x}_j, \vec{x}_s) = e^{-i\omega t(\vec{x}_j, \vec{x}_s)}$ are used, and only the manner in which $t(\vec{x}_j, \vec{x}_s)$ is estimated is adapted to use relative distances perpendicular to the plane wavefront (Fig. 1b) instead of distances to potential source locations (Fig. 1d). Standard MFP is delay-and-sum beamforming, and the difference lies in whether plane waves or curved wavefronts are used (Bucker, 1976). The simple analytical Green's function used in standard MFP can be understood in two ways: They are the wavefields emmitted by point sources (the impulse responses), if the medium is an acoustic, isotropic, homogeneous half-space. They also represent a phase shift (or time-delay), if convolved with a waveform.

Understanding beamforming as convolution leads to another way of conceptualising MFP. We rewrite the beampower score (eq. 3), omitting the variables $(\omega, \vec{x}_j, \vec{x}_s)$ for readability, as

$$B = \sum_{\omega} \sum_{j} \sum_{k \neq j} s_j^* d_k^* d_j s_k = \sum_{\omega} \sum_{j} \sum_{k \neq j} (s_j^* s_k)(d_k^* d_j). \tag{6}$$

Here, $d_k^* d_j$ is the correlation of the recorded wavefields and $s_j^* s_k$ the correlation of the synthetic wavefields for each station pair k, j. The cross-correlations $s_j^* s_k$ constitute the relative phase shifts to be applied in standard MFP and the "matching" of wavefields in MFP is exactly this: convolution of their correlation wavefields, where the sum of the convolution is the mismatch measure.

This is particulary relevant, because it also makes the close connection between MFP and the interferometry-based localisation strategy apparent, and gives a different perspective to the insights provided by Bowden et al. (2021). In both approaches, cross-correlation functions of recorded data and of synthetic data are computed and compared against each other. The main difference between them lies in how exactly cross-correlation functions are computed and how the (mis-)fit between

the two is evaluated. It is then not surprising that MFP results are a good starting model for interferometry-based localisation (Igel et al., 2021a); in a very real sense MFP *is* interferometry-based localisation, without data processing, e.g., waveform-normalisation or stacking, and a different mismatch measure. Bowden et al. (2021) have described this connection more mathematically: starting from cross-correlation beamforming (Ruigrok et al., 2017), a simple change in the order of operations - from shifting waveforms first and then computing the cross-correlation coefficient to first computing the correlation function and then measuring at the corresponding time lag - creates an equivalency (under certain conditions) between MFP and interferometry-based source inversion. This description and the one we introduce above result in the same realisation. Fundamentally, only two approaches for locating sources of the ambient seismic field exist: polarisation analysis (Fig. 1a) and approaches that exploit exactly wavefield-coherency across stations (Fig. 1b-d). That beamforming, MFP, and interferometry-based localisation are essentially the same may not be intuitive at first, especially considering the strikingly different sketches to illustrate them (Fig. 1b-d), and the different language both communities use.

To retrieve "reliable" cross-correlation functions of the recorded data in ambient noise seismology, processing and stacking over time is common (Bensen et al., 2007). MFP foregoes processing of seismograms for stability entirely, allowing for high time-resolution and avoiding artefacts potentially introduced by the processing (Fichtner et al., 2020). Importantly though, the mismatch measure employed in MFP does not allow iterative inversion by source-strength perturbation, because convolution (or correlation) does not account for amplitude mismatch. If signals are in phase, increasing amplitudes of one results in linearly-scaling beampowers regardless of how well the waveforms fit. It is clear that both communities may benefit from each other, as is one of the fundamental arguments by Bowden et al. (2021). It is fairly straight-forward to employ strategies of the ambient seismic noise community to "improve" the correlation functions $d_k^* d_j$. A detailed analysis of the advantages and disadvantages this would bring, and what exactly "improving" would mean in the context of MFP is beyond the scope of this paper. Similarly, increasing the accuracy of MFP in a seismological context and discussing its fundamental ideas and limitations, as is the intent of this paper, will benefit developments in the larger field of ambient seismic noise localisation.

2.5 Limitations of MFP

Above, we have already explored the advantages and limitations of using numerically computed synthetic wavefields (Fig. 2) and amplitudes (Fig. 3) in MFP, as well as the emergence of striped

interference patterns for narrowband sources (Fig. 2). MFP shows further undesired behaviour under certain conditions that we encounter in real-world applications. Some of these are more straight-forward to understand in the conceptual framework of convolution introduced above.

2.5.1 Source-Station Geometry

Standard MFP becomes plane-wave beamforming for very large distances between source and array, because accounting for curved wavefronts has negligible impact on travel times. In that case, the lessons learned in beamforming, e.g., what wavelengths are resolvable without aliasing, apply one-to-one (Rost & Thomas, 2002). When MFP is considered as an approach, the source-station geometry should be such that accounting for curved wavefronts actually has useful impact on the results, i.e., the difference in expected travel times compared to plane waves is much larger than the expected measurement error. Because MFP is not bound to the plane-wave assumption, there is no meaningful difference between treating a collection of stations as an array or a network. Still, the inter-station distance should not be much smaller than the investigated wavelength or incoherent noise may prevent being able to reliably resolve the source location.

Closely related to these considerations is that high waveform coherency is required across stations, regardless of approach. In standard MFP or beamforming, i.e., $s(\omega, \vec{x}_j, \vec{x}_s) = e^{-i\omega t(\vec{x}_j, \vec{x}_s)}$, coherency means retaining the exact shape of the waveforms across stations, because waveforms are simply shifted in time. In nMFP, waveform coherency takes a slightly different meaning, because elastic wave propagation can change the shape of recorded waveforms significantly. So instead, waveforms need to be coherent after elastic wave propagation effects have been accounted for, in nMFP via synthetic Green's functions for Earth structure.

Station density has direct impact on the retrieved beampower distribution that is worth pointing out explicitly. In a synthetic test, we place additional stations on the right side (Fig. 4a). The beampower distribution shows a bias towards the top-left, caused simply by the presence of more stations that recorded the signal in the bottom-right. While in the ideal scenario here, the exact source location is still resolved correctly, interpreting this distribution without prior knowledge of the sources in a real-world application is challenging. This bias in MFP results follows directly from understanding MFP as the sum over convolutions of correlated wavefields, as described above. Regions with higher station density are then inherently weighted higher and cause the observed effect.

This goes beyond increased resolution due to better suppression of incoherent noise, and is an

effect that essentially all real-world applications of MFP will have to take into consideration. We have tested two possible approaches to correct for this without success. Introducing a coherency-weight where stations that recorded similar waveforms are down-weighted to counter-act the described behaviour, does not improve the retrieved beampower distribution. This approach further lessens the advantage that multiple measurements at similar positions can reduce impact of incoherent noise. A different approach may be to homogenise the station distribution, but this often excludes high-quality stations from the analysis, especially for permanent arrays.

2.5.2 Multiple Sources

Single sources can cause prominent interference patterns, if they are narrowband (Fig. 2c,d), which depend on station geometry and frequency band. This leads to even more complex, secondary interference when multiple sources are active at the same time. In a synthetic test, we place two narrowband sources that excite identical wavefields simultaneously (Fig. 4b). The second source is placed such that it lies at the edge of a sidelobe of the first source (Fig. 2d). From the retrieved distribution of beampowers it is not at all obvious that two and only two sources are active here, and instead this may be misidentified as a single source close to the left array (Fig. 4b). The new beampower peak is entirely an interference artefact. This smearing of resolved source locations clearly relates to the wavelength of the investigated waves, and similar issues are well-known in the beamforming community (more on that in section 2.5.4). When the two sources placed are broadband instead (Fig. 4c), one may interpret the beampower distribution as two sources. The true locations are however not recovered, with a smaller error for the closer source. Similar problems, such as smeared beampower distributions can occur for single sources that move during the investigated time frame (Li et al., 2021).

2.5.3 Time window length

In MFP, a choice has to be made on how long of a time window is analysed. The basic requirement is that the time needs to be long enough to record the correlated wavefield propagating across all stations, which can be estimated roughly from expected wave velocities. Because MFP is based on correlation wavefields, by default the entirety of the chosen time window influences the result. This is easier to understand with the delay-and-sum concept, where waveforms are shifted in time and summed. Because the entire waveforms are used to compute the sum, all of the waveform plays a role. This limits the time resolution of MFP and has implications depending on the type

of source one aims to investigate. If a source is exciting energy repeatedly, the wavefield contains more and more of that source's energy the longer the time window is and thus gets weighted higher and higher. This is very useful for stationary "noise" sources. For impulsive sources that act rarely, this can be a disadvantage and time windows should be chosen as small as possible for them. To address this issue, the concept of a windowing function as developed for the interferometry-based localisation strategy (Bowden et al., 2021), may be an opportunity to increase MFP's time resolution even further in the future.

2.5.4 Quantifying resolution

For plane-wave beamforming, the impact of an array's geometry on its resolution capability is well studied, and expressed by the array-response function (Rost & Thomas, 2002). The array response is calculated by computing the beampower distribution for a single synthetic incident wave. At first glance, this looks like a four-dimensional problem: two dimensions for the horizontal slowness of the synthetic wave, and two for the horizontal slownesses sampled during beamforming. The array's response can be shown to be only dependent to relative slownesses, i.e., the array response is simply shifted to be centered on the slowness of the synthetic wave and does not change its shape (Rost & Thomas, 2002). The resolution problem for plane-wave beamforming is therefore reduced to two dimensions and the bias on beampower distributions can be visualised and understood for all possible single incident waves from investigating a single synthetic wave. Analysing relative slownesses is equivalent to a synthetic wave with slowness 0 s/km, which is why this slowness is most commonly used. In practice, the array response is usually considered only qualitatively as a guide to which relative slownesses show sidelobes or have poor resolution (e.g., Rost & Thomas, 2002; Ruigrok et al., 2017; Löer et al., 2018).

In MFP, a similar simplification to only consider relative synthetic source locations does not apply, because the investigated wavefield is curved. Therefore, the resolution problem has eight dimensions: the location in three dimensions and the medium velocity for both the synthetic source and the sampled sources. Other simplifications are necessary to be able to communicate the beampower resolution. If one considers sources at the surface, as done in the analysis above (Figs. 2 – 4), the problem reduces to six dimensions. To further reduce dimensions, a choice of synthetic source location has to be made. Because the choice of location is important for the resulting beampower distribution, there is no obvious choice that is commonly accepted in MFP studies. Instead, the location should be chosen such that the resulting beampower distribution demonstrates relevant

effects.

In our analysis, we have made choices of synthetic source locations for demonstration purposes (Figs. 2 – 4). The resulting beampower distributions give an impression of beampower bias similar to array-response functions in plane-wave beamforming. This is possible, because we only investigate sources at the surface and our approach avoids sampling velocity by incorporating an Earth velocity model in the computation of $s(\omega, \vec{x}_j, \vec{x}_s)$, which combined reduces the problem down to two dimensions. In particular, the choice of the synthetic source location can have significant impact on the beampower distribution. Multiple sources complicate this further and may cause dominant sidelobe artefacts that are impossible to identify and address in practice, especially if only a limited frequency band is available (Fig. 4b). This aspect is also relevant for plane-wave beamforming but usually ignored. It is important to keep the above assumptions and simplifications in mind when interpreting an array's response or our synthetic tests. They do not provide comprehensive insight into the highly complex interactions across all dimensions of the problem. To address this, ideally a single metric would exist that expresses the entirety of beampower distribution bias for every possible source location, including multiple simultaneously acting sources.

Xu & Mikesell (2022) approach the resolution problem by applying singular-value-decomposition to MFP. This allows to compute resolution and covariance matrices for a given array geometry at each potential source location. However, they do not address how the bias due to interference when multiple sources act simultaneously should be taken into account in practice. For interferometry-based localisation, Xu et al. (2020) show that the presence of multiple sources can result in not being able to resolve all of them. This also applies to MFP (Fig. 4b). Additionally, the array geometry acts as a filter on the true source distribution in MFP, which should be taken into account during interpretation (Xu & Mikesell, 2022).

One approach to remove the imprint of the array geometry on the MFP results is deconvolution of the array response from the beampower distribution. Originally developed in radio astronomy, the CLEAN algorithm (Högbom, 1974) has been applied to plane-wave beamforming of ambient seismic noise, enabling identification of previously undetected phases (Gal et al., 2016). Even though our approach reaches the resolution problem dimensionality of plane-wave beamforming (under the assumptions and simplifications described above), the CLEAN algorithm relies on the same key assumption that the array response relies on: that a single synthetic source of a given horizontal slowness sufficiently describes the bias on the beampower distribution. For MFP, we have shown this to be potentially incorrect (Fig. 4b), which should be considered if designing an adaptation of

the CLEAN algorithm to MFP.

The considerations above briefly demonstrate the, in our view, most important limitation of MFP: the concrete interpretation of individual MFP results. Interpretation seems quite challenging when either stations are distributed heterogeneously or multiple sources are acting and may have interfering sidelobe patterns. Both conditions are true for most real-world applications, especially in the context of ambient seismic noise. This is one of the main reasons other beamformers and processing techniques are being developed across disciplines (e.g., Capon, 1969; Schmidt, 1986; Cox et al., 1987; Cox, 2000; Gal et al., 2014, 2016; Zhu et al., 2020). In future work, exploring their applicability to and further developing them in the context of elastic waves propagating in complex Earth structure seems like a clear way forward. Significant advances on the resolution problem would have impact way beyond the seismological community.

3 Demonstration on real data

We demonstrate nMFP on two real data examples.

3.1 2008 Chino Hills Earthquake

First, we benchmark nMFP with an earthquake in Southern California, the $M_W = 5.4$ Chino Hills earthquake of 2008-07-29 (Fig. 5). When applying the standard MFP approach, with an assumed velocity $v = 3.2$ km/s (the best fit in the synthetic test in Fig. 2), we find a relatively good location of the earthquake with 7.7 km distance to the location in the CI catalog (Fig. 5a, SCEDC, 2013). The good fit here confirms what other authors have found before: standard MFP can already perform quite well in seismological studies (Gal et al., 2018; Umlauft & Korn, 2019; Umlauft et al., 2021). When we replace $s(\omega, \vec{x}_j, \vec{x}_s)$ with numerical Green's functions for an explosive source mechanism, we at first find a decrease in location accuracy (Fig. 5b). The retrieved location is 18.3 km away from the CI location. When we incorporate the moment tensor solution from the CI catalog (SCEDC, 2013), straight-forward to do with nMFP, we find an improvement in location accuracy with a distance of only 1.9 km to the CI location (Fig. 5c). This demonstrates one of the potential use cases for MFP with numerical Green's functions: Searching for the best-fitting moment tensor may help constrain the source mechanism of unknown weak sources. A related strategy has been employed by Umlauft et al. (2021). The authors flipped the sign of waveforms, based on visual inspection and expert judgement, before applying MFP. The spatial distribution of whether a

waveform had to be flipped or not to increase waveform-coherency across stations, gives hints on the radiation pattern and thus source mechanism of the seismic sources, in their case stick-slip tremor at the base of a glacier. In such a scenario, where clear identification of phase arrivals is difficult, our approach may be more systematic and help give improved estimates of the source mechanism.

In the case of strong earthquakes, such as this example, the usefulness of MFP is limited. Other approaches that rely on data abstraction are routinely applied and provide more precise results that allow uncertainty quantification (Li et al., 2020). We chose this example, exactly because we can compare with results from such trusted methods, i.e., the catalog location, which allows us to confirm the validity of nMFP.

3.2 Secondary Microseism

In a second example, we further showcase the usefulness of nMFP. We locate seismic sources in the secondary microseism frequency band (0.13 to 0.15 Hz) in the Northeastern Atlantic and Mediterrenean Sea using 342 stations distributed over Europe during the first week of February 2019 (Fig. 6). Three snapshots of beampower distributions are compared against hindcasts of significant wave height (WaveWatch III, Ardhuin et al., 2011). On first order, we find a good match between the standard approach (left), nMFP (middle), and the distribution of significant wave height (right) for all snapshots, at least with $v = 3.2$ km/s in the standard approach. First, we focus on the results for the standard approach.

For the first snapshot (Fig. 6a,c), the results using the standard approach correlate well with significant wave heights regardless of chosen velocity, and seismic sources are located West of the British Isles. In the second example, however, we find considerable differences in the beampower distribution depending on chosen velocity (Fig. 6d). The increased ocean activity to the North and West of the Iberian Peninsula matches best with significant wave heights for velocities $v = 3.0$ or $v = 3.2$ km/s (Fig. 6d,f). With $v = 2.8$ km/s an entirely different region, to the West of France and South of the British Isles, is located as the dominant source (Fig. 6d). Similarly for the third snapshot, we find a clear region of high beampowers in the Mediterranean Sea, West of Corsica, that corresponds to significant wave heights only for $v = 3.2$ km/s (Fig. 6g,i).

This suggests that $v = 3.2$ km/s is a resonable choice of seismic wave velocity for the analysed frequency band, reaffirming our synthetic analysis (Fig. 2) and our choice in the earthquake example above (Fig. 5). We claim that seismic sources of the secondary microseism should roughly co-locate with significant wave heights as an argument for the validity of this choice. This is resonable, because

the common explanation for the secondary microseism mechanism is that ocean gravity waves at the water surface, propagating in roughly opposite direction, interact and cause a standing wave that generates a vertically-propagating pressure wavefield in the water column. This pressure wavefield then interacts with the ocean bottom, generating seismic waves in the solid Earth (Hasselmann, 1963; Ardhuin et al., 2015). In the open oceans, significant wave heights alone have been shown to be insufficient for explaining seismic wave generation, because they are not necessarily coinciding with gravity waves propagating in roughly opposite direction (Ardhuin et al., 2019). Because our study area is fairly close to the coast of Europe, coastal reflections are the most likely explanation for the fit we find between seismic source locations and significant wave heights.

The choice of the "best" velocity for standard MFP relies heavily on exactly such prior knowledge and assumptions. Without prior knowledge about the study target, velocity would instead be searched as a parameter and the velocity corresponding to the highest beampower would be picked for the analysis (e.g., Gradon et al., 2019). Still, even then assumptions on the nature of possible sources are made to simplify the problem, e.g., no distributed simultaneously acting sources. Deviation from such assumptions can have significant impact on the retrieved beampowers and complicate the decision (Fig. 4b). Our example for the secondary microseism demonstrates the complexity of beampower distributions one encounters in a real world application that would need to be interpreted when making a choice of v (Fig. 6, left). Without relying on the assumption of seismic wave generation by the secondary microseism mechanism and other prior knowledge, it is impossible to judge whether any of the tested velocities is a better choice for standard MFP and may lead to significantly different interpretation of the results. All of the tested velocities are resonable Rayleigh wave velocities, and deciding on one of them beforehand would include prior knowledge about what kind of shallow crustal structure is expected or dominant, e.g., sedimentary basins or crystalline basement.

nMFP makes a similar assumption by choosing a velocity model to compute synthetic wavefields for (Fig. 6 middle). We do, however, not base our selection of velocity model on how well MFP results match our expectations, which is fundamentally what testing of velocities in standard MFP achieves. Instead, we rely on the validity of the velocity model and computational strategy for computing wavefields, which have been developed by the seismological community over decades. This is an important assumption in its own right, but a profoundly different one. nMFP removes the need to search velocity as a parameter and reduces the solution space of MFP by one dimension (velocity) while incorporating complex Earth structure and elastic wave propagating at the same time

through the use of an Earth model. These considerations give a different perspective to the main idea and biggest strength of nMFP: when we incorporate the complexity of elastic wave propagation through Green's functions computed numerically for a realistic model of Earth structure, we free ourselves from assumptions about the study target. Similar considerations apply to the earthquake example above. Importantly, this also means that nMFP likely performs worse when the real velocity structure in the study area deviates significantly from the Earth model used, an effect that is more pronounced for higher frequencies. Currently, we rely on an axisymmetric PREM model, which is a severe limitation. In future works, heterogeneous 3D models of Earth structure should be incorporated in the computation of Green's function databases utilised in nMFP.

The similarity between the standard approach (with $v = 3.2$ km/s) and nMFP is generally high (Fig. 6 left and middle). This result is not surprising for a number of reasons and should be understood as an argument in favour of our approach, as discussed above. The sources we image here are generally far away from most stations and towards one direction, West. The difference in waveforms recorded across all stations then becomes relatively small. If sources were closer to all stations, as e.g., for the Chino Hills earthquake (Fig. 5), improving the accuracy of the synthetic wavefield has larger impact. As mentioned above, the Green's function we rely on are based on an axisymmetric PREM Earth. Therefore we do not yet incorporate the full complexity of elastic wave propagation in this demonstration, which increases the similarity to the standard approach. Particularly relevant are the European shelf areas and the structural contrast between oceanic and continental crust (Le Pape et al., 2021). Finally, because we investigate the secondary microseism, we are limited to a narrow frequency band and cannot benefit from utilising broadband seismic waveforms. We find only slight differences between standard MFP with $v = 3.2$ km/s and nMFP, e.g., that beampower distributions retrieved with nMFP are more focused on specific regions compared to the standard approach.

We do not yet feel comfortable in judging whether these differences are certain to be an improvement in source estimation due to the resolution problem discussed in section 2.5.4. Our synthetic tests (Fig. 2) and the Chino Hills earthquake example (Fig. 5) suggest that our approach can be more precise in locating sources. For the secondary microseism, however, we have to be careful with interpreting the observed patterns, as we have also demonstrated in synthetic tests (Fig. 4b). If nMFP will prove to be more precise also for microseisms, we may find that seismic waves are excited in specific regions in the oceans and not distributed homogeneously beneath storm systems. It is important to note here that for now we use an explosion source mechanism for the synthetic wave-

fields to locate the microseism, which we have already shown to be inadequate for an earthquake (Fig. 5). In the future, we require a strategy to describe and incorporate a source mechanisms appropriate for microseisms. Such a mechanism should, in addition to the vertical forcing, incorporate the periodic nature of the source in a physical manner, and how excitation strength depends on local sea bed structure, such as topography and sediment thickness. Some insight in how that could be approached has been given by Gualtieri et al. (2020) and this is certainly an attractive prospect and may help better understand the exact excitation mechanism.

4 Conclusions

Matched Field Processing (MFP) is generalized beamforming for arbitrary wavefields, removing the need for the plane-wave assumption. It is one of the current approaches to locating sources of ambient seismic noise (Fig. 1). In this study, we advance MFP to better incorporate elastic wave propagation in the Earth by using Green's functions numerically computed for a model of Earth structure directly as the synthetic wavefield that the data is matched against. We call this approach *numerical MFP* (nMFP).

When amplitudes are considered in MFP, results are biased by amplitude effects such as geometrical spreading and anelastic attenuation. In the standard approach, this is usually neglected through spectral whitening of the synthetic wavefield. We find that this strategy performs best for us as well, and that trying to correct for spreading and attenuation via an amplitude term, as has been suggested before, may not be advisable (Fig. 3). This is especially the case for nMFP, where multiple wave types can be considered simultaneously.

Two examples on real data showcase the potential of nMFP (Figs. 5, 6). In principle, we can use it to search for the source mechanism of a seismic source, as suggested by the improved source location after incoporating the earthquake's moment tensor (Fig. 5). This could be particularly useful in the context of tremor activity, where source mechanism determination is challenging with classical approaches. In a second example, we locate sources of the secondary microseism in the Northern Atlantic and Mediterrenean Sea (Fig. 6). Results from nMFP match the standard approach's results closely, likely due to source geometry, narrow frequency band, and our reliance on Green's functions computed for an axisymmetric Earth. nMFP retains the advantage that is not biased by author choice of a medium velocity, and potentially provides higher resolution.

We clarify conceptual approaches to MFP and its close connection to the interferometry-based

localisation. The striking similarity between them suggests that it may be a worthwhile endeavour to unify them in the future, or at least provide a framework to let the different communities benefit from each others' work. On a conceptual level, Beamforming, MFP, and the interferometry-based localisation strategy all rely on quantifiyng the mismatch of correlation wavefields. MFP in particular would benefit tremendously from a universally applicable approach for quantifying its resolution. The lack of such a measure is currently its major disadvantage.

Future advances specifically for nMFP could be on more precise Green's functions databases, or investigating the performance of beamformers particularly for elastic wave propagation. With current tools, there is the potential for reasonably sized databases that incorporate full 3D Earth structure when limitting source locations to be only at the surface. More precise Green's functions should also incorporate a better description of the microseism source mechanism, different for the primary and secondary microseism. nMFP could improve MFP with few and sparsely distributed stations, because it is less reliant on waveform-coherency across seismic stations in its strict sense. While seismometer density is improving worldwide consistently, regions with sparse deployments and without purposefully built arrays are still the norm. Furthermore, tremor activity such as volcanic tremor is often challenging to locate with classical approaches. Particularly in such regions and study targets, nMFP is a powerful strategy for localising the origin of seismic energy.

Data and Materials

We provide all data and code used to generate the figures in this paper to make it entirely reproducible (`https://github.com/seismology-hamburg/schippkus_hadziioannou_2022`). There, we also provide a minimal working MFP example based on synthetic data and the standard approach to make the method more accessible for students and researchers interested in MFP. The MFP computations in this study rely on Python code developed for this work, which we make available under MIT license at `https://github.com/seismology-hamburg/matched_field_processing`.

Seismic data used in this study was provided by network operators of international, national, and regional seismic networks in Europe and America (Royal Observatory of Belgium, 1985; Department of Earth and Environmental Sciences, Geophysical Observatory, University of Munchen, 2001; Swiss Seismological Service (SED) At ETH Zurich, 1983; California Institute of Technology and United States Geological Survey Pasadena, 1926; Charles University in Prague (Czech) et al., 1973; GEUS Geological Survey of Denmark and Greenland, 1976; Dublin Institute for Advanced Studies, 1993;

RESIF, 1995; Institut De Physique Du Globe De Paris (IPGP) & Ecole Et Observatoire Des Sciences De La Terre De Strasbourg (EOST), 1982; British Geological Survey, 1970; GEOFON Data Centre, 1993; Federal Institute for Geosciences and Natural Resources, 1976; Scripps Institution of Oceanography, 1986; None, 1965; Albuquerque Seismological Laboratory (ASL)/USGS, 1988; INGV Seismological Data Centre, 1997; Instituto Dom Luiz (IDL) - Faculdade de Ciências da Universidade de Lisboa, 2003; MedNet Project Partner Institutions, 1988; ZAMG - Zentralanstalt für Meterologie und Geodynamik, 1987; Istituto Nazionale di Oceanografia e di Geofisica Sperimentale - OGS, 2016; KNMI, 1993; Norsar, 1971; Polish Academy of Sciences (PAN) Polskiej Akademii Nauk, 1990; Instituto Português do Mar e da Atmosfera, I.P., 2006; RESIF, 2018; University of Leipzig, 2001; Institut fuer Geowissenschaften, Friedrich-Schiller-Universitaet Jena, 2009; San Fernando Royal Naval Observatory (ROA) et al., 1996) and accessed through ORFEUS, EIDA, and IRIS via obspy (Krischer et al., 2015).

Colormaps used in this study are perceptually uniform (Crameri et al., 2020).

Acknowledgements

The authors thank Anya Reading and one anonymous reviewer for insightful comments and suggestions that helped significantly improve the manuscript. The authors thank Josefine Umlauft and Jonas Igel for insightful discussions of the ideas presented in this paper. This work was partially funded by the Emmy Noether program (HA7019/1-1) of the German Research Foundation (DFG).

References

Aki, K., 1957. Space and time spectra of stationary stochastic waves, with special reference to microtremors, *Bulletin of the Earthquake Research Institute*, **35**, 415–457.

Albuquerque Seismological Laboratory (ASL)/USGS, 1988. Global Seismograph Network - IRIS/USGS.

Ardhuin, F., Stutzmann, E., Schimmel, M., & Mangeney, A., 2011. Ocean wave sources of seismic noise, *Journal of Geophysical Research*, **116**(C9), C09004–21.

Ardhuin, F., Gualtieri, L., & Stutzmann, E., 2015. How ocean waves rock the Earth: Two mechanisms explain microseisms with periods 3 to 300 s, *Geophysical Research Letters*, **42**(3), 765–772.

Ardhuin, F., Gualtieri, L., & Stutzmann, E., 2019. Physics of Ambient Noise Generation by Ocean Waves, in *Seismic Ambient Noise*, pp. 69–108, Cambridge Univ. Press.

Baggeroer, A., Kuperman, W., & Mikhalevsky, P., 1993. An overview of matched field methods in ocean acoustics, *IEEE Journal of Oceanic Engineering*, **18**(4), 401–424.

Bensen, G. D., Ritzwoller, M. H., Barmin, M. P., Levshin, A. L., Lin, F., Moschetti, M. P., Shapiro, N. M., & Yang, Y., 2007. Processing seismic ambient noise data to obtain reliable broad-band surface wave dispersion measurements, *Geophysical Journal International*, **169**(3), 1239–1260.

Bowden, D. C., Sager, K., Fichtner, A., & Chmiel, M., 2021. Connecting beamforming and kernel-based noise source inversion, *Geophysical Journal International*, **224**(3), 1607–1620.

Brenguier, F., Campillo, M., Hadziioannou, C., Shapiro, N. M., Nadeau, R. M., & Larose, E., 2008. Postseismic relaxation along the San Andreas fault at Parkfield from continuous seismological observations., *Science (New York, N.Y.)*, **321**(5895), 1478–1481.

Brenguier, F., Boué, P., Ben-Zion, Y., Vernon, F. L., Johnson, C. W., Mordret, A., Coutant, O., Share, P. E., Beaucé, E., Hollis, D., & Lecocq, T., 2019. Train traffic as a powerful noise source for monitoring active faults with seismic interferometry, *Geophysical Research Letters*, **46**(16), 9529–9536.

Brienzo, R. K. & Hodgkiss, W. S., 1993. Broadband matched-field processing, *The Journal of the Acoustical Society of America*, **94**(5), 2821–2831.

British Geological Survey, 1970. Great Britain Seismograph Network.

Bucker, H. P., 1976. Use of calculated sound fields and matched-field detection to locate sound sources in shallow water, *The Journal of the Acoustical Society of America*, **59**(2), 368–373.

Burtin, A., Bollinger, L., Vergne, J., Cattin, R., & Nábělek, J. L., 2008. Spectral analysis of seismic noise induced by rivers: A new tool to monitor spatiotemporal changes in stream hydrodynamics, *Journal of Geophysical Research: Solid Earth*, **113**(B5).

California Institute of Technology and United States Geological Survey Pasadena, 1926. Southern California Seismic Network.

Campillo, M. & Roux, P., 2015. Crust and Lithospheric Structure - Seismic Imaging and Monitoring with Ambient Noise Correlations, in *Treatise on Geophysics*, pp. 391–417, Elsevier.

Capon, J., 1969. High-resolution frequency-wavenumber spectrum analysis, *Proceedings of the IEEE*, **57**(8), 1408–1418.

Charles University in Prague (Czech), Institute of Geonics, Institute of Geophysics, Academy of Sciences of the Czech Republic, Institute of Physics of the Earth Masaryk University (Czech), & Institute of Rock Structure and Mechanics, 1973. Czech regional seismic network.

Corciulo, M., Roux, P., Campillo, M., Dubucq, D., & Kuperman, W. A., 2012. Multiscale matched-field processing for noise-source localization in exploration geophysics, *GEOPHYSICS*, **77**(5), KS33–KS41.

Cox, H., 2000. Multi-rate adaptive beamforming (MRABF), in *Proceedings of the IEEE Sensor Array and Multichannel Signal Processing Workshop*, pp. 306–309, ORINCON Corporation, Arlington, United States.

Cox, H., Zeskind, R., & Owen, M., 1987. Robust adaptive beamforming, *IEEE Transactions on Acoustics, Speech, and Signal Processing*, **35**(10), 1365–1376.

Crameri, F., Shephard, G. E., & Heron, P. J., 2020. The misuse of colour in science communication, *Nature Communications*, pp. 1–10.

Dean, T., 2019. The seismic signature of rain, *ASEG Extended Abstracts*, **2018**(1), 1–8.

DeMuth, G., 1977. Frequency domain beamforming techniques, in *ICASSP '77. IEEE International Conference on Acoustics, Speech, and Signal Processing*, vol. 2, pp. 713–715.

Department of Earth and Environmental Sciences, Geophysical Observatory, University of Munchen, 2001. BayernNetz.

D'Spain, G. L., Murray, J. J., Hodgkiss, W. S., Booth, N. O., & Schey, P. W., 1999. Mirages in shallow water matched field processing, *The Journal of the Acoustical Society of America*, **105**(6), 3245–3265.

Dublin Institute for Advanced Studies, 1993. Irish National Seismic Network.

Dziewonski, A. M. & Anderson, D. L., 1981. Preliminary reference Earth model, *Physics of the Earth and Planetary Interiors*, **25**(4), 297–356.

Ermert, L., Villaseñor, A., & Fichtner, A., 2016. Cross-correlation imaging of ambient noise sources, *Geophysical Journal International*, **204**(1), 347–364.

Ermert, L., Sager, K., Nissen-Meyer, T., & Fichtner, A., 2021. Multi-frequency inversion of global ambient seismic sources, *Geophysical Journal International*.

Federal Institute for Geosciences and Natural Resources, 1976. German Regional Seismic Network (GRSN).

Fichtner, A., Stehly, L., Ermert, L., & Boehm, C., 2017. Generalized interferometry – I: Theory for interstation correlations, *Geophysical Journal International*, **208**(2), 603–638.

Fichtner, A., Bowden, D., & Ermert, L., 2020. Optimal processing for seismic noise correlations, *Geophysical Journal International*, **223**(3), 1548–1564.

Fuchs, F., Bokelmann, G. H. R., & the AlpArray Working Group, 2017. Equidistant spectral lines in train vibrations, *Seismological Research Letters*, **89**(1), 56–66.

Gal, M. & Reading, A. M., 2019. Beamforming and polarisation analysis, in *Seismic Ambient Noise*, pp. 32–72, Cambridge Univ. Press.

Gal, M., Reading, A. M., Ellingsen, S. P., Koper, K. D., Gibbons, S. J., & Näsholm, S. P., 2014. Improved implementation of the fk and Capon methods for array analysis of seismic noise, *Geophysical Journal International*, **198**(2), 1045–1054.

Gal, M., Reading, A. M., Journal, S. E. G., & 2016, 2016. Deconvolution enhanced direction of arrival estimation using one-and three-component seismic arrays applied to ocean induced microseisms, *Geophysical Journal International*, **206**(1), 345–359.

Gal, M., Reading, A. M., Rawlinson, N., & Schulte-Pelkum, V., 2018. Matched field processing of three-component seismic array data applied to Rayleigh and Love microseisms, *Journal of Geophysical Research: Solid Earth*, **42**(4), 765–19.

GEOFON Data Centre, 1993. GEOFON Seismic Network.

GEUS Geological Survey of Denmark and Greenland, 1976. Danish Seismological Network.

Gibbons, S. J., Harris, D. B., Kvaerna, T., & Dodge, D. A., 2017. Comprehensive Seismic Detection and Estimation Using Matched Field Processing, Technical Report AD1056994, Air Force Resarch Laboratory, Kirtland Air Force Base, NM.

840 Gradon, C., Moreau, L., Roux, P., & Ben-Zion, Y., 2019. Analysis of surface and seismic sources in
841 dense array data with match field processing and Markov chain Monte Carlo sampling, *Geophysical*
842 *Journal International*, **218**(2), 1044–1056.

843 Gualtieri, L., Bachmann, E., Simons, F. J., & Tromp, J., 2020. The origin of secondary microseism
844 Love waves., *Proceedings of the National Academy of Sciences of the United States of America*,
845 **117**(47), 29504–29511.

846 Hadziioannou, C., Larose, E., Baig, A., Roux, P., & Campillo, M., 2011. Improving temporal
847 resolution in ambient noise monitoring of seismic wave speed, *Journal of Geophysical Research*,
848 **116**(B7), B08310–10.

849 Hasselmann, K., 1963. A statistical analysis of the generation of microseisms, *Reviews of Geophysics*,
850 **1**(2), 177–210.

851 Heimann, S., Kriegerowski, M., Isken, M., Cesca, S., Daout, S., Grigoli, F., Juretzek, C., Megies,
852 T., Nooshiri, N., Steinberg, A., Sudhaus, H., Vasyura-Bathke, H., Willey, T., & Dahm, T., 2017.
853 Pyrocko - An open-source seismology toolbox and library.

854 Högbom, J. A., 1974. Aperture synthesis with a non-regular distribution of interferometer baselines,
855 *Astronomy and Astrophysics Supplement Series*, **15**, 417.

856 Hu, W., Barthelmie, R. J., Letson, F., & Pryor, S. C., 2019. Seismic noise induced by wind turbine
857 operation and wind gusts, *Seismological Research Letters*, **91**(1), 427–437.

858 Hutko, A. R., Bahavar, M., Trabant, C., Weekly, R. T., Fossen, M. V., & Ahern, T., 2017. Data
859 Products at the IRIS-DMC: Growth and Usage, *Seismological Research Letters*, **88**(3), 892–903.

860 Igel, J., Bowden, D., Sager, K., & Fichtner, A., 2021a. Imaging noise sources: Comparing and
861 combining a matched-field processing technique with finite-frequency noise source inversions, in
862 *EGU General Assembly 2021*, online.

863 Igel, J. K., Ermert, L. A., & Fichtner, A., 2021b. Rapid finite-frequency microseismic noise source
864 inversion at regional to global scales, *Geophysical Journal International*, **227**(1), 169–183.

865 INGV Seismological Data Centre, 1997. Rete Sismica Nazionale (RSN).

Institut De Physique Du Globe De Paris (IPGP) & Ecole Et Observatoire Des Sciences De La Terre De Strasbourg (EOST), 1982. GEOSCOPE, French Global Network of broad band seismic stations.

Institut fuer Geowissenschaften, Friedrich-Schiller-Universitaet Jena, 2009. Thüringer Seismologisches Netz.

Instituto Dom Luiz (IDL) - Faculdade de Ciências da Universidade de Lisboa, 2003. University of Lisbon Seismic Network.

Instituto Português do Mar e da Atmosfera, I.P., 2006. Portuguese National Seismic Network.

Istituto Nazionale di Oceanografia e di Geofisica Sperimentale - OGS, 2016. North-east italy seismic network.

Johnson, C. W., Meng, H., Vernon, F. L., & Ben-Zion, Y., 2019. Characteristics of ground motion generated by wind interaction with trees, structures, and other surface obstacles, *Journal of Geophysical Research: Solid Earth*, **124**(8), 8519–8539.

Juretzek, C. & Hadziioannou, C., 2016. Where do ocean microseisms come from? A study of Love-to-Rayleigh wave ratios, *Journal of Geophysical Research: Solid Earth*, **121**(9), 6741–6756.

Juretzek, C. & Hadziioannou, C., 2017. Linking source region and ocean wave parameters with the observed primary microseismic noise, *Geophysical Journal International*, **211**(3), 1640–1654.

KNMI, 1993. Netherlands Seismic and Acoustic Network.

Krim, H. & Viberg, M., 1996. Two decades of array signal processing research: The parametric approach, *IEEE Signal Processing Magazine*, **13**(4), 67–94.

Krischer, L., Megies, T., Barsch, R., Beyreuther, M., Lecocq, T., Caudron, C., & Wassermann, J., 2015. ObsPy: A bridge for seismology into the scientific Python ecosystem, *Computational Science & Discovery*, **8**(014003).

Krischer, L., Hutko, A. R., van Driel, M., Stähler, S., Bahavar, M., Trabant, C., & Nissen-Meyer, T., 2017. On-Demand Custom Broadband Synthetic Seismograms, *Seismological Research Letters*, **88**(4), 1127–1140.

Le Pape, F., Craig, D., & Bean, C. J., 2021. How deep ocean-land coupling controls the generation of secondary microseism Love waves, *Nature Communications*, **12**(1), 2332.

Li, F., Zhu, F., Zhang, Y., Zhang, B., Li, W., & Luo, W., 2021. Synthetic adaptive matched field processing for moving source with a horizontal line array, *The Journal of the Acoustical Society of America*, **149**(2), 1138–1146.

Li, L., Tan, J., Schwarz, B., Staněk, F., Poiata, N., Shi, P., Diekmann, L., Eisner, L., & Gajewski, D., 2020. Recent Advances and Challenges of Waveform-Based Seismic Location Methods at Multiple Scales, *Reviews of Geophysics*, **58**(1), e2019RG000667.

Liu, Y., Yue, Y., Luo, Y., & Li, Y., 2021. Effects of high-speed train traffic characteristics on seismic interferometry, *Geophysical Journal International*, **227**(1), 16–32.

Löer, K., Riahi, N., & Saenger, E. H., 2018. Three-component ambient noise beamforming in the Parkfield area, *Geophysical Journal International*, **213**(3), 1478–1491.

Longuet-Higgings, M. S., 1950. A theory of the origin of microseisms, *Philosophical Transactions of the Royal Society of London A Mathematical, Physical and Engineering Sciences*, **243**(857), 1–35.

Lu, Y., Stehly, L., Paul, A., & the AlpArray Working Group, 2018. High-resolution surface wave tomography of the European crust and uppermost mantle from ambient seismic noise, *Geophysical Journal International*, **214**(2), 1136–1150.

MedNet Project Partner Institutions, 1988. Mediterranean Very Broadband Seismographic Network (MedNet).

eds Nakata, N., Gualtieri, L., & Fichtner, A., 2019. *Seismic Ambient Noise*, Cambridge University Press, Cambridge.

Nissen-Meyer, T., van Driel, M., Stähler, S. C., Hosseini, K., Hempel, S., Auer, L., Colombi, A., & Fournier, A., 2014. AxiSEM: Broadband 3-D seismic wavefields in axisymmetric media, *Solid Earth*, **5**(1), 425–445.

None, 1965. International Miscellaneous Stations (IMS).

Norsar, 1971. NORSAR Station Network.

Paul, A., Campillo, M., Margerin, L., Larose, E., & Derode, A., 2005. Empirical synthesis of time-asymmetrical Green functions from the correlation of coda waves, *Journal of Geophysical Research*, **110**(B8), B08302–13.

Polish Academy of Sciences (PAN) Polskiej Akademii Nauk, 1990. Polish Seismological Network.

RESIF, 1995. RESIF-RLBP French Broad-band Network, RESIF-RAP Strong Motion Network and Other Seismic Stations in Metropolitan France.

RESIF, 2018. CEA/DASE Broad-band Permanent Network in Metropolitan France.

Riahi, N. & Gerstoft, P., 2015. The seismic traffic footprint: Tracking trains, aircraft, and cars seismically, *Geophysical Research Letters*, **42**(8), 2674–2681.

Riahi, N., Bokelmann, G., Sala, P., & Saenger, E. H., 2013. Time-lapse analysis of ambient surface wave anisotropy: A three-component array study above an underground gas storage, *Journal of Geophysical Research: Solid Earth*, **118**(10), 5339–5351.

Rost, S. & Thomas, C., 2002. Array Seismology: Methods and Applications, *Reviews of Geophysics*, **40**(3), 2–1–2–27.

Royal Observatory of Belgium, 1985. Belgian seismic network.

Ruigrok, E., Gibbons, S., & Wapenaar, K., 2017. Cross-correlation beamforming, *Journal of Seismology*, **21**(3), 495–508.

Sager, K., Boehm, C., Ermert, L., Krischer, L., & Fichtner, A., 2018. Sensitivity of Seismic Noise Correlation Functions to Global Noise Sources, *Journal of Geophysical Research: Solid Earth*, **123**(8), 6911–6921.

San Fernando Royal Naval Observatory (ROA), Universidad Complutense De Madrid (UCM), Helmholtz-Zentrum Potsdam Deutsches GeoForschungsZentrum (GFZ), Universidade De Evora (UEVORA, Portugal), & Institute Scientifique Of RABAT (ISRABAT, Morocco), 1996. The Western Mediterranean BB Seismic Network.

SCEDC, 2013. Southern California Earthquake Center.

Schimmel, M. & Gallart, J., 2003. The use of instantaneous polarization attributes for seismic signal detection and image enhancement, *Geophysical Journal International*, **155**(2), 653–668.

946 Schimmel, M., Stutzmann, E., Ardhuin, F., & Gallart, J., 2011. Polarized Earth's ambient micro-
947 seismic noise, *Geochemistry, Geophysics, Geosystems*, **12**(7).

948 Schippkus, S., Zigone, D., Bokelmann, G. H. R., & the AlpArray Working Group, 2018. Ambient-
949 noise tomography of the wider Vienna Basin region, *Geophysical Journal International*, **215**(1),
950 102–117.

951 Schippkus, S., Garden, M., & Bokelmann, G., 2020. Characteristics of the Ambient Seismic Field on
952 a Large-N Seismic Array in the Vienna Basin, *Seismological Research Letters*, **91**(5), 2803–2816.

953 Schmidt, R., 1986. Multiple emitter location and signal parameter estimation, *IEEE Transactions*
954 *on Antennas and Propagation*, **34**(3), 276–280.

955 Scripps Institution of Oceanography, 1986. Global Seismograph Network - IRIS/IDA.

956 Sergeant, A., Chmiel, M., Lindner, F., Walter, F., Roux, P., Chaput, J., Gimbert, F., & Mordret, A.,
957 2020. On the Green's function emergence from interferometry of seismic wave fields generated
958 in high-melt glaciers: Implications for passive imaging and monitoring, *The Cryosphere*, **14**(3),
959 1139–1171.

960 Sethian, J. A., 1999. Fast Marching Methods, *SIAM Review*, **41**(2), 199–235.

961 Shapiro, N. M., Campillo, M., Stehly, L., & Ritzwoller, M. H., 2005. High-resolution surface-wave
962 tomography from ambient seismic noise., *Science*, **307**(5715), 1615–1618.

963 Smith, K. & Tape, C., 2019. Seismic Noise in Central Alaska and Influences From Rivers, Wind,
964 and Sedimentary Basins, *Journal of Geophysical Research: Solid Earth*, **124**(11), 11678–11704.

965 Soares, C. & Jesus, S. M., 2003. Broadband matched-field processing: Coherent and incoherent
966 approaches, *The Journal of the Acoustical Society of America*, **113**(5), 2587–2598.

967 Stammler, K. & Ceranna, L., 2016. Influence of wind turbines on seismic records of the Gräfenberg
968 array, *Seismological Research Letters*, **87**(5), 1075–1081.

969 Swiss Seismological Service (SED) At ETH Zurich, 1983. National seismic networks of switzerland.

970 Tolstoy, A., 1989. Sensitivity of matched field processing to sound-speed profile mismatch for vertical
971 arrays in a deep water Pacific environment, *The Journal of the Acoustical Society of America*,
972 **85**(6), 2394–2404.

973 Umlauft, J. & Korn, M., 2019. 3-D fluid channel location from noise tremors using matched field
974 processing, *Geophysical Journal International*, **219**(3), 1550–1561.

975 Umlauft, J., Lindner, F., Roux, P., Mikesell, T. D., Haney, M. M., Korn, M., & Walter, F. T., 2021.
976 Stick-Slip Tremor Beneath an Alpine Glacier, *Geophysical Research Letters*, **48**(2).

977 University of Leipzig, 2001. SXNET Saxon Seismic Network.

978 van Driel, M., Krischer, L., Stähler, S. C., Hosseini, K., & Nissen-Meyer, T., 2015. Instaseis: Instant
979 global seismograms based on a broadband waveform database, *Solid Earth*, **6**(2), 701–717.

980 Wapenaar, K., Draganov, D., Snieder, R., Campman, X., & Verdel, A., 2010. Tutorial on seismic
981 interferometry: Part 1 — Basic principles and applications, *GEOPHYSICS*, **75**(5), 75A195–
982 75A209.

983 Xu, Z. & Mikesell, T. D., 2022. Estimation of Resolution and Covariance of Ambient Seismic Source
984 Distributions: Full Waveform Inversion and Matched Field Processing, *Journal of Geophysical*
985 *Research: Solid Earth*, **127**(6), e2022JB024374.

986 Xu, Z., Mikesell, T. D., Umlauft, J., & Gribler, G., 2020. Rayleigh-wave multicomponent
987 crosscorrelation-based source strength distribution inversions. Part 2: A workflow for field seismic
988 data, *Geophysical Journal International*, **222**(3), 2084–2101.

989 Yong, P., Liao, W., Huang, J., Li, Z., & Lin, Y., 2019. Misfit function for full waveform inversion
990 based on the Wasserstein metric with dynamic formulation, *Journal of Computational Physics*,
991 **399**, 108911.

992 ZAMG - Zentralanstalt für Meterologie und Geodynamik, 1987. Austrian seismic network.

993 Zhu, G., Wang, Y., & Wang, Q., 2020. Matched Field Processing Based on Bayesian Estimation,
994 *Sensors*, **20**(5), 1374.

995 Ziane, D. & Hadziioannou, C., 2019. The contribution of multiple scattering to Love wave generation
996 in the secondary microseism, *Geophysical Journal International*, **217**(2), 1108–1122.

Figures

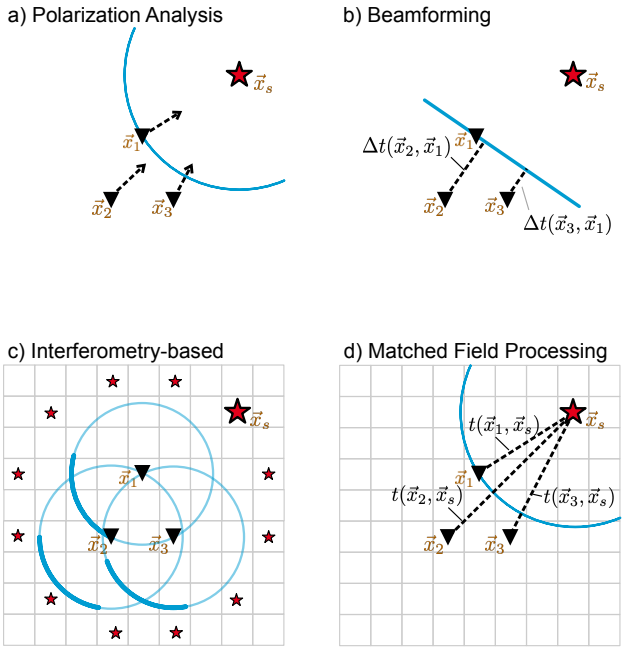

Figure 1: Current approaches to locating sources of the ambient seismic field. Wavefronts are marked blue. a) Polarization Analysis: the polarization of the wavefield on individual three-component seismometers gives an indication of direction of propagation. Triangulation allows source localisation. b) Beamforming: seismograms on multiple stations are shifted in time corresponding to candidate plane-waves, and summed over. c) Interferometry-based strategy: compare cross-correlation functions computed from seismograms of multiple stations with synthetically computed cross-correlation functions for a given source distribution. Cross-correlation functions are sensitive to the source distribution and are asymmetric (indicated by thickness of wavefront), if sources are distributed heterogeneously. d) Matched Field Processing is generalized beamforming, sampling candidate source locations instead of assuming plane waves, which allows for curved wavefronts.

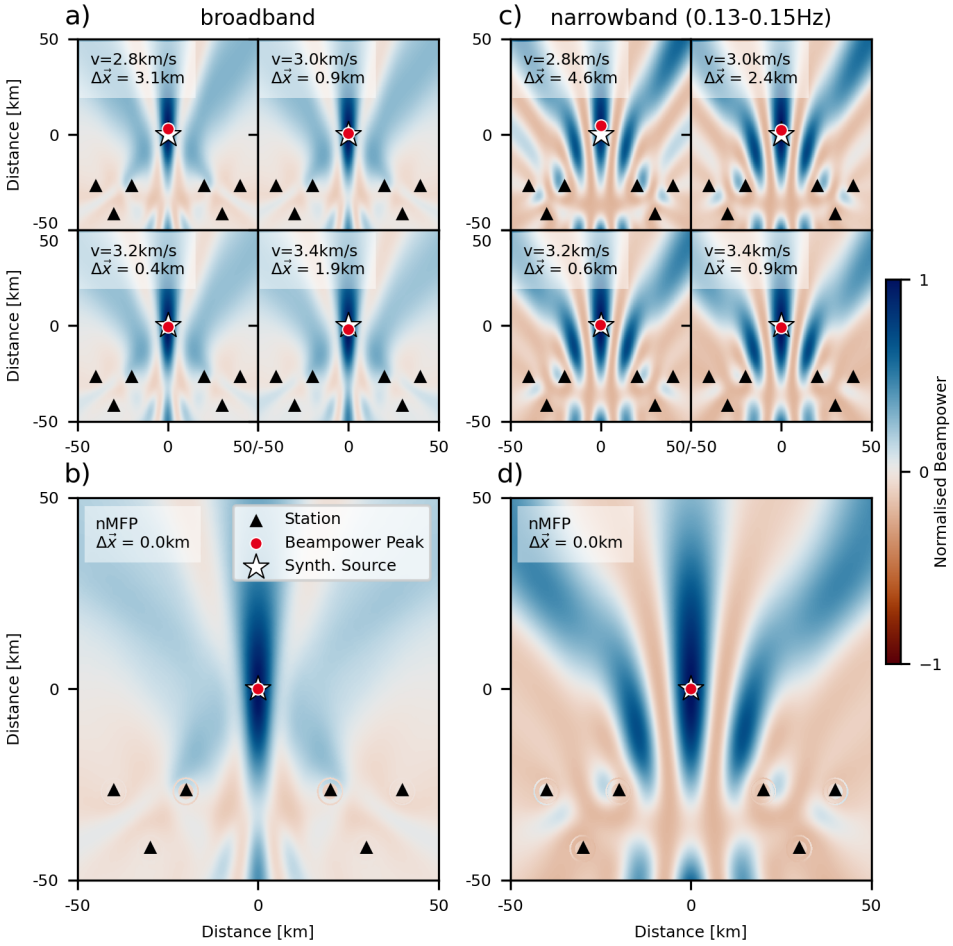

Figure 2: Synthetic demonstration for two three-station arrays locating an explosion source. The grid point with the highest beampower is the estimated source location (red circle), the white star marks the synthetic source. Note the difference between the two $\Delta\vec{x}$ with standard MFP (top row). Left: broadband source. a) Standard approach, with travel times estimated for constant velocity. The retrieved source location is sensitive to the chosen velocity. b) Our approach, with numerical Green's functions as synthetic wavefields (nMFP). Source is precisely located. Right: narrowband source (0.13-0.15Hz). c) Standard approach. Emergence of sidelobes due to interference. d) nMFP in the same narrow frequency band and the source is precisely located.

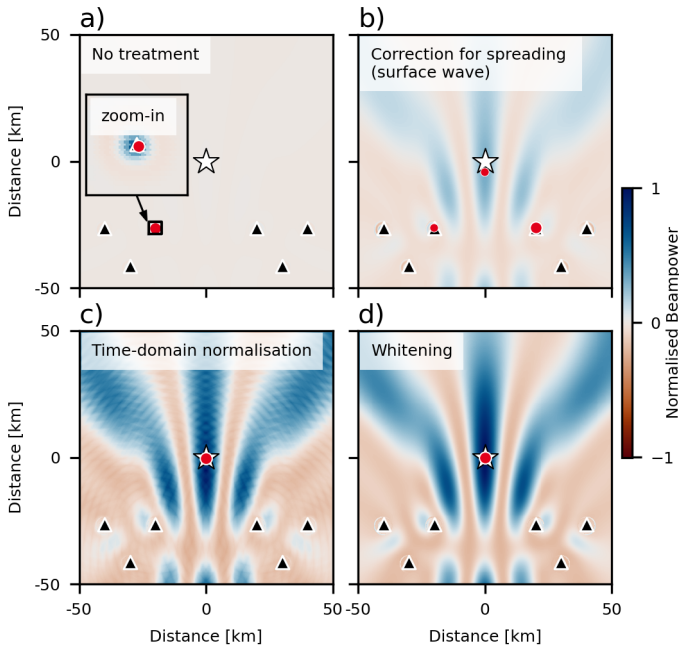

Figure 3: Strategies for treating amplitude information. a) No amplitude treatment. b) Correction for geometrical spreading of surface waves. Smaller red circles mark local beampower maxima. c) Time-domain normalisation of numerical Green's function (GF). d) Spectral whitening (frequency-domain normalisation) of numerical Green's function (GF).

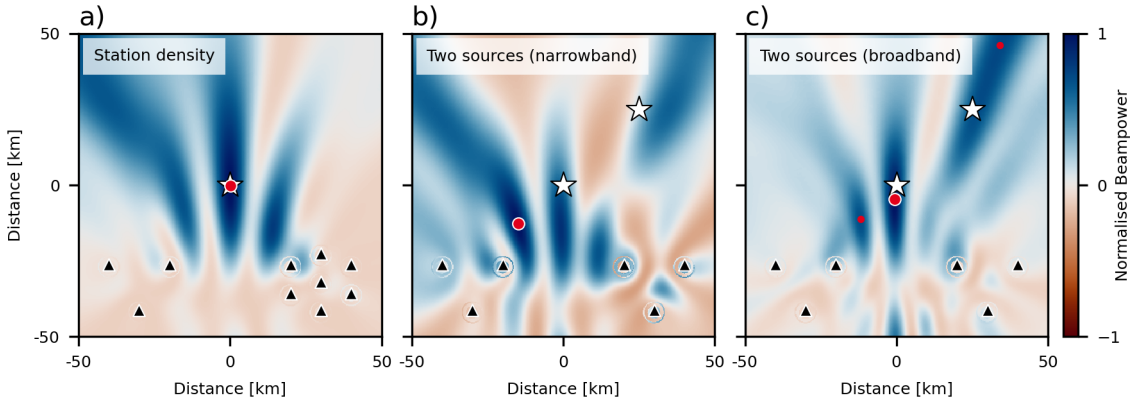

Figure 4: Some limitations of MFP, regardless of Green's function formulation. a) Impact of station density. Increased number of stations on one side results in bias of potential source locations. True source location is still resolved. b) Two narrowband (0.13 to 0.15 Hz) sources active at the same time (white stars). Beampower distribution does not represent source locations well. Global beampower maximum (red circle) is an interference artefact. c) Same as b), but for broadband sources. Beampower maxima lie closer to the synthetic source locations, but still not well-resolved. Smaller red circles mark local beampower maxima.

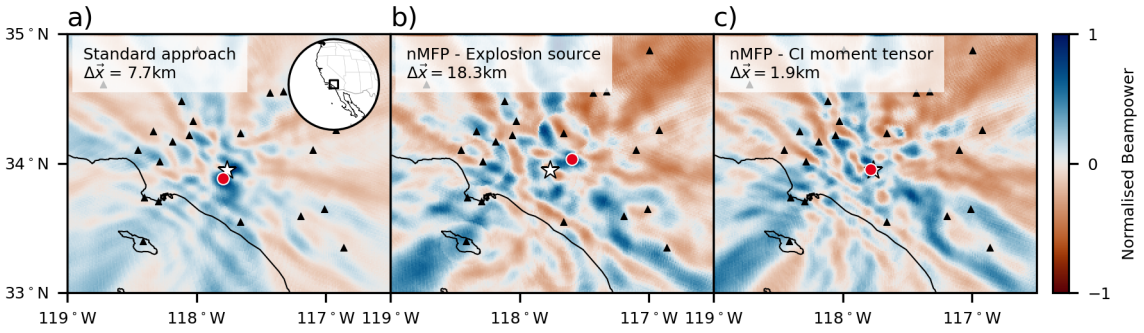

Figure 5: Location of the 2008-07-29 Chino Hills earthquake from the CI catalog (white star, SCEDC, 2013) and MFP (red circle) at 15.5km depth. MFP results were obtained using stations of the Southern California Seismic Network (black triangles) and frequencies from 0.1 to 0.2 Hz. a) Beampower distribution with simple analytical Green's functions, assuming $v = 3.2$ km/s. 7.7 km distance to the CI location. b) Beampower distribution using numerical Green's functions for an explosive source mechanism. 18.3 km distance to the CI location. c) Beampower distribution using numerical Green's functions for the moment tensor solution in the CI catalog (SCEDC, 2013). Accounting for the source mechanism of the earthquake improves the resolved location, performing better than standard MFP (1.9 km distance to the CI location).

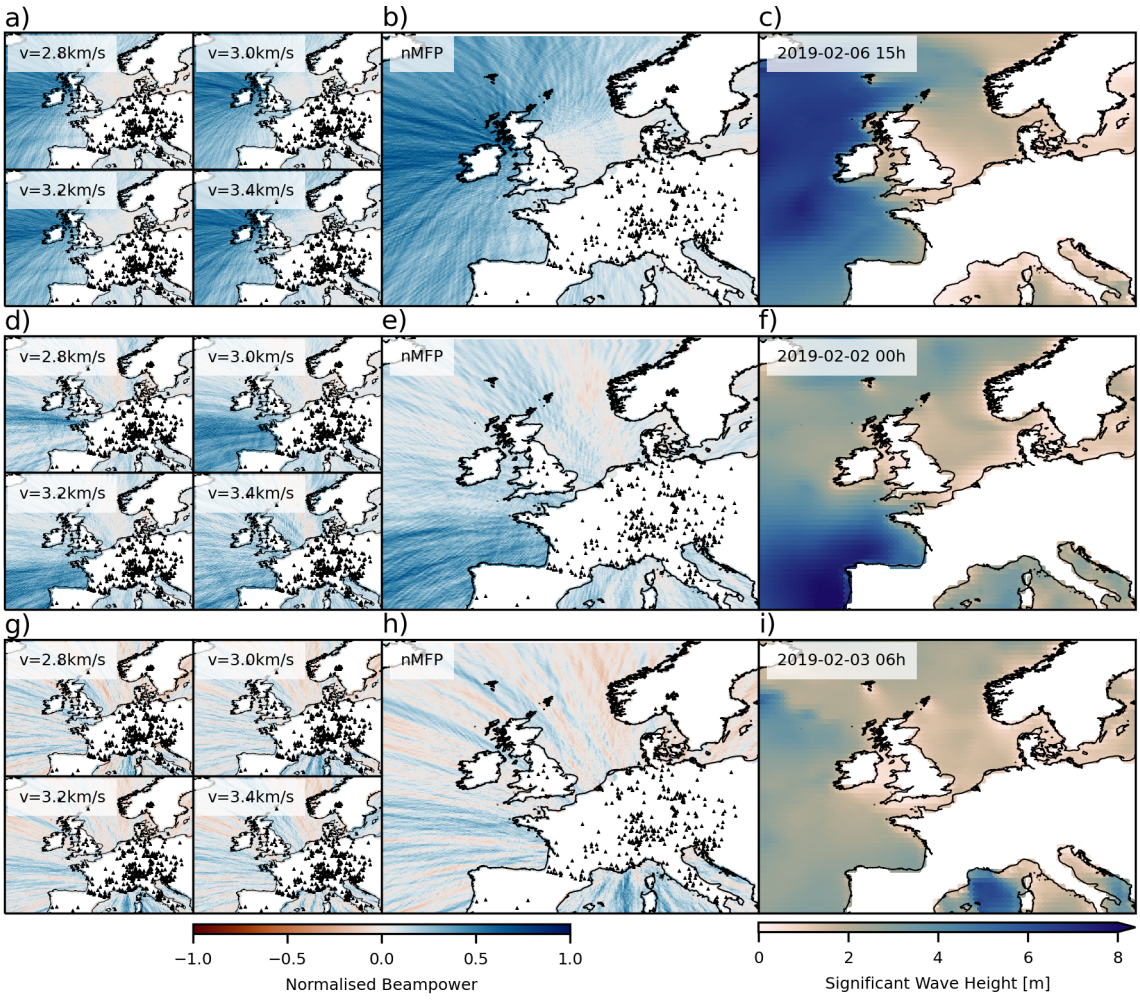

Figure 6: MFP results for the secondary microseism (0.13 to 0.15 Hz) during the first week of February 2019 for three time windows (rows). 342 stations distributed over Europe were used (black triangles). Left: MFP using analytical Green's functions for different chosen velocities v. Significant impact of choice on beampower distribution. Middle: MFP using numerically computed Green's functions (nMFP). Right: Maps of significant wave height hindcasts, provided by WaveWatch III (Ardhuin et al., 2011).